Universal fluctuating regime in triangular chromate antiferromagnets

K. Somesh,[1] Y. Furukawa,[2] G. Simutis,[3] F. Bert,[3] M. Prinz-Zwick,[4] N. Büttgen,[4] A. Zorko,[5,6] A. A. Tsirlin,[7,*] P. Mendels,[3,†] and R. Nath[1,‡]

[1]*School of Physics, Indian Institute of Science Education and Research, Thiruvananthapuram-695551, India*
[2]*Ames Laboratory and Department of Physics and Astronomy, Iowa State University, Ames, Iowa 50011, USA*
[3]*Université Paris-Saclay, CNRS, Laboratoire de Physique des Solides, 91405 Orsay, France*
[4]*Experimental Physics V, Center for Electronic Correlations and Magnetism, University of Augsburg, D-86159 Augsburg, Germany*
[5]*Jožef Stefan Institute, Jamova c. 39, SI-1000 Ljubljana, Slovenia*
[6]*Faculty of Mathematics and Physics, University of Ljubljana, SI-1000 Ljubljana, Slovenia*
[7]*Experimental Physics VI, Center for Electronic Correlations and Magnetism, University of Augsburg, 86135 Augsburg, Germany*

(Received 22 June 2021; revised 7 September 2021; accepted 9 September 2021; published 22 September 2021)

We report x-ray diffraction, magnetic susceptibility, heat capacity, ^{1}H nuclear magnetic resonance (NMR), and muon spin relaxation (μSR) measurements, as well as density-functional band-structure calculations for the frustrated $S = 3/2$ triangular lattice Heisenberg antiferromagnet (TLHAF) α-$HCrO_2$ (trigonal, space group: $R\bar{3}m$). This compound undergoes a clear magnetic transition at $T_N \simeq 22.5$ K, as seen from the drop in the muon paramagnetic fraction and concurrent anomalies in the magnetic susceptibility and specific heat capacity. Local probes (NMR and μSR) reveal a broad regime with slow fluctuations down to $0.7\,T_N$, this temperature corresponding to the maximum in the μSR relaxation rate and in the NMR wipe-out. From the comparison with $NaCrO_2$ and α-$KCrO_2$, the fluctuating regime and slow dynamics below T_N appear to be hallmarks of the TLHAF with *ABC* stacking. We discuss the role of interlayer frustration, which may have impacted recent spin-liquid candidates with triangular geometry.

DOI: 10.1103/PhysRevB.104.104422

I. INTRODUCTION

Experimental realization of quantum spin liquid (QSL) remains one of the major challenges in condensed-matter physics [1,2]. An identification of this exotic entangled state in real-world materials could open the way to understanding and utilizing fractionalized excitations, which are particularly interesting in the context of quantum computing [3]. Theoretical studies established several promising settings for the QSL that were indeed proposed [4] in antiferromagnets with the kagome [5], triangular [6], and honeycomb [7] structures, all of them based on the two-dimensional interaction geometries.

Recent work on triangular antiferromagnets [6] exposed the $AYbX_2$ compound family (A = Na, K and X = O, S, Se) as the largest stock of the QSL candidates known to date. In fact, all members of this family evade long-range magnetic order [8–13], while some of them additionally show spectral signatures of fractionalized spinon excitations [14] or excitations of a Dirac QSL [15,16]. One potentially important but hitherto neglected feature of these compounds is the *ABC*-type stacking of their triangular layers that causes frustration of the interlayer couplings, as shown in Fig. 1. Each magnetic site is coupled to three sites of the adjacent layer. This arrangement prevents simple ferro- or antiferromagnetic order along c.

Here, we explore the effect of this intra- and interlayer frustration using the $ACrO_2$ chromates. These compounds are convenient model systems that contain semiclassical spins $\frac{3}{2}$ and, thanks to the half-filled t_{2g} shell of Cr^{3+}, feature isotropic Heisenberg interactions within the triangular planes. Such an interaction regime is known to induce 120° order in the plane, which is indeed observed in $LiCrO_2$ [17–20], but other members of the same family do not show a clear magnetic ordering. In $NaCrO_2$, a transition at $T_N \simeq 41$ K is followed by a broad fluctuating regime with slow dynamics extending down to $T^* \simeq 30$ K [21] for which the occurrence of Berezinskii-Kosterlitz-Thouless (BKT) was suggested [22]. On the other hand, α-$HCrO_2$ with the shortest interlayer distance was recently claimed to evade magnetic order and lie in the vicinity of a spin-liquid phase [23]. Using a combination of thermodynamic and local probes applied to α-$HCrO_2$, we show that in fact all these chromates—$NaCrO_2$, α-$HCrO_2$, as well as α-$KCrO_2$ [24]—develop a very similar phenomenology. They enter a broad universal fluctuating regime below T_N, followed by the formation of a static and likely incommensurate spin state below T^*. Our findings reveal a new mechanism of creating fluctuating spin-liquid-like states that reside on the triangular planes but crucially rely on the interlayer frustration.

II. METHODS

A polycrystalline sample of α-$HCrO_2$ was prepared by a hydrothermal method. It involves two steps. First, the intermediate oxide Cr_8O_{21} was prepared by heating CrO_3

*altsirlin@gmail.com
†philippe.mendels@universite-paris-saclay.fr
‡rnath@iisertvm.ac.in

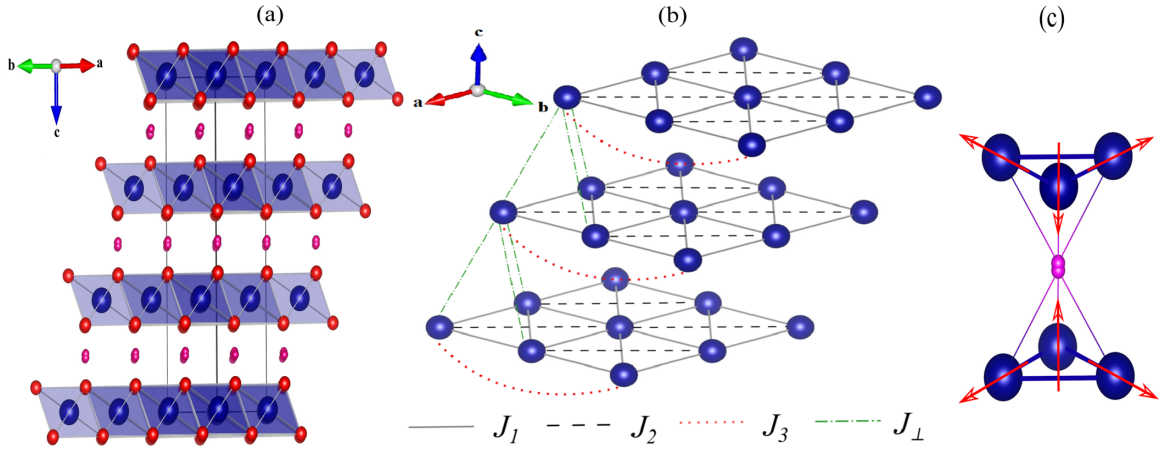

FIG. 1. (a) Crystal structure of α-$HCrO_2$ consisting of triangular layers formed by CrO_6 octahedra and H atoms at the interstitial sites. (b) Triangular Cr layers showing possible exchange couplings J_1, J_2, J_3, and $J_\perp$ between the Cr^{3+} ions. (c) Coupling of H with three Cr^{3+} ions from each layer where spins are arranged in a 120° structure.

(Aldrich, 99.99% pure) granules for 12 h at 250 °C in air. In the second step, the intermediate product was crushed into fine powder, put into a 1 M LiOH solution in deionized water, heated at 200 °C in a teflon-lined stainless steel autoclave for about one week, and subsequently furnace-cooled. The phase purity of the product was confirmed by powder x-ray diffraction (XRD) using a PANalytical x-ray diffractometer (Cu $K\alpha$ radiation, $\lambda_{av} = 1.541\,82$ Å). The temperature-dependent powder XRD measurement was performed over the temperature range $15 \leqslant T \leqslant 300$ K using the low-temperature attachment (Oxford Phenix) to the diffractometer.

Magnetization (M) measurements were performed as a function of temperature (T) and applied field (H) using a superconducting quantum interference device (MPMS-3, Quantum Design). Heat capacity [$C_p(T)$] as a function of T and H was measured on a small piece of sintered pellet using the relaxation technique in the physical property measurement system (PPMS, Quantum Design).

The NMR measurements were carried out using pulsed NMR techniques on ^{1}H (nuclear spin $I = 1/2$ and gyromagnetic ratio $\gamma_N/2\pi = 42.575$ MHz/T) nuclei in the temperature range $1.6 \leqslant T \leqslant 250$ K and at different radio frequencies. The spectra were obtained either by Fourier transform (FT) of the NMR echo signal or by sweeping the magnetic field. The NMR shift $K = (\nu - \nu_{ref})/\nu_{ref}$ was determined by measuring the resonance frequency of the sample (ν) with respect to nonmagnetic reference H_2O (resonance frequency ν_{ref}). The ^{1}H spin-lattice relaxation rate ($1/T_1$) was measured by the conventional inversion recovery method. The spin-spin relaxation rate ($1/T_2$) was measured through the decay of the echo integral with variable spacing between the $\pi/2$ and π pulses.

The muon spin rotation/relaxation (μSR) experiments were carried out at the πM_3 beam line using the GPS spectrometer at the Paul Scherrer Institute (PSI), Switzerland [25]. The zero-field (ZF) and the weak transverse-field (wTF) μSR measurements were performed at temperatures ranging from ∼1.5 to 50 K. The 100% spin-polarized μ^+ (spin-1/2 and gyromagnetic ratio $\gamma_\mu = 135.5$ MHz/T) with the momentum of ∼28.6 MeV/c were implanted into the sample. Because of their positive charge, muons come at rest in well-defined sites where their electrostatic energy is minimized, i.e., in oxides typically 1 Å away from an oxygen O^{2-} site. They usually interact with surrounding moments through a dipolar coupling. In a paramagnetic state, the electronic moments fluctuate fast (∼10^{-12} s) on the μSR timescale, and the static field sensed by the muons has only a nuclear origin with a typical value of a few Gauss, while dynamical electronic fields lead to motional narrowing. On the contrary, when electronic moments slow down, the evolution of the ZF polarization with time witnesses both their dynamics and freezing. At the base temperature ($T \ll T_N$), very high counting statistics (∼115 events) were taken in order to track the fast-decaying polarization measured in zero-field, where the contribution from static electronic moments dominates.

Density-functional (DFT) band-structure calculations were performed in the FPLO code [26] using the Perdew-Burke-Ernzerhof flavor of the exchange-correlation potential [27]. Correlation effects in the Cr 3d shell were taken into account of the mean-field DFT+U level using the on-site Coulomb repulsion $U_d = 2$ eV, Hund's coupling $J_d = 1$ eV, and atomic limit for the double-counting correction [28,29]. Experimental structural parameters for $LiCrO_2$ [30], $NaCrO_2$ [31], and α-$KCrO_2$ [31] have been used. In the case of α-$HCrO_2$, the position of hydrogen remains somewhat uncertain. We thus considered two limiting cases: (i) hydrogen placed in the middle between the CrO_2 layers, with the $R\bar{3}m$ symmetry preserved; (ii) hydrogen displaced toward one of the layers. In the latter case, the symmetry is reduced to $R3m$, and the individual CrO_6 octahedra are slightly distorted, because the Cr-O distances can be shorter or longer depending on how strongly the oxygen atom binds to the hydrogen. Room-temperature atomic positions from Ref. [32] have been used, as they feature the largest distortion and allow one to test its effect on magnetism. Exchange parameters J_{ij} and single-ion

anisotropy D enter the spin Hamiltonian,

$$\mathcal{H} = \sum_{\langle ij \rangle} J_{ij} \mathbf{S}_i \mathbf{S}_j - \sum_i D\left(S_i^z\right)^2, \tag{1}$$

where the summation is over atomic pairs $\langle ij \rangle$, and $S = \frac{3}{2}$. The parameters of this Hamiltonian were obtained by a mapping procedure [33] from total energies of magnetically ordered states.

III. RESULTS

A. X-ray diffraction

To confirm the phase purity and to check the presence of any structural distortions, powder XRD data were collected at various temperatures. The Rietveld refinements of the XRD patterns were executed using the FULLPROF software package [34] with the initial parameters taken from Ref. [32]. Figure 2 presents the powder XRD patterns at 300 and 15 K along with the Rietveld fits. At room temperature, all the peaks could be indexed based on the space group $R\bar{3}m$ (No. 166) suggesting phase purity of the sample. A small difference between the experimental and calculated intensities at $2\theta \sim 38^\circ$ is likely due to preferred orientation effects expected in a layered compound. The obtained lattice parameters at room temperature are $a = b = 2.9836(1)$ Å, $c = 13.4232(1)$ Å, and unit-cell volume $V_{\text{cell}} \simeq 103.48$ Å^3, which are comparable with the previous report [32]. No extra features or peaks were observed in the XRD scans implying the absence of any structural transitions down to 15 K. On the other hand, around 30 K both lattice parameters (a and c) clearly deviate from their anticipated low-temperature behavior [see Fig. 2(c)]. Such weak kinks, humps, and changes of slope are commonly observed in magnetic compounds in the vicinity of their magnetic transitions, where lattice symmetry does not change but a magnetoelastic coupling leads to anomalies in thermal expansion [35,36].

The temperature variation of the lattice constants (a and c) and unit-cell volume (V_{cell}) as shown in Fig. 2(c) are found to decrease monotonically upon cooling down to $T \approx 45$ K. $V_{\text{cell}}(T)$ above 45 K was fitted by the equation [37]

$$V(T) = \gamma U(T)/K_0 + V_0, \tag{2}$$

where V_0 is the cell volume in the zero-temperature limit, K_0 is the bulk modulus, and γ is the Grüneisen parameter. $U(T)$ is the internal energy, which can be derived in terms of the Debye approximation as

$$U(T) = 9nk_{\text{B}}T\left(\frac{T}{\theta_{\text{D}}}\right)^3 \int_0^{\theta_{\text{D}}/T} \frac{x^3}{e^x - 1} dx. \tag{3}$$

Here, n is the number of atoms in the unit cell and k_{B} is the Boltzmann constant. Using this approximation [see Fig. 2(c)], the Debye temperature (θ_{D}) and other parameters were estimated to be $\theta_{\text{D}} = 195(9)$ K, $\gamma/K_0 = 2.95(7) \times 10^{-5}$ Pa^{-1}, and $V_0 \simeq 102.8(7)$ Å^3.

B. Magnetization

Previous magnetic susceptibility $\chi(T)$ and ^{1}H NMR measurements were restricted to temperatures above the possible magnetic ordering [38,39]. An antiferromagnetic transition at $T_{\text{N}} \sim 25$ K has been reported from the heat capacity measurements [40].

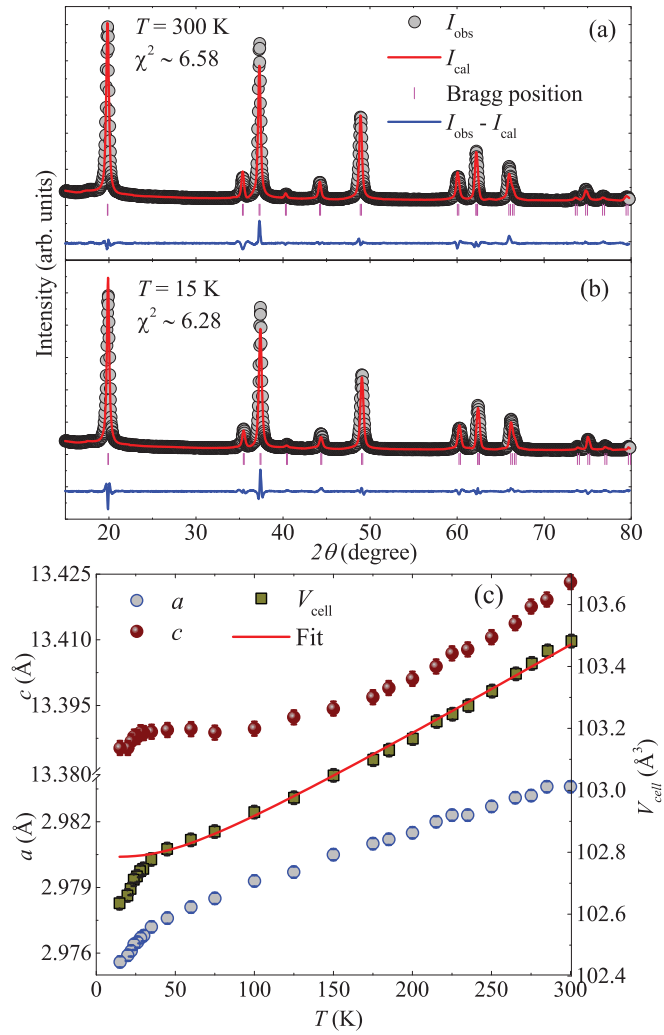

FIG. 2. Powder XRD data measured at (a) $T = 300$ and (b) $T = 15$ K. The red solid line represents the Rietveld fit of the data. The Bragg positions are indicated by pink vertical bars, and the solid blue line at the bottom denotes the difference between the experimental and calculated intensities. (c) The variation of the lattice parameters (a, c, and V_{cell}) as a function of temperature. The solid line denotes the fit of the $V_{\text{cell}}(T)$ by Eq. (2).

The temperature-dependent magnetic susceptibility $\chi(T)$ ($\equiv M/H$) measured in an applied field of 0.5 T is shown in Fig. 3. As expected in the paramagnetic regime, $\chi(T)$ increases with decreasing temperature in a Curie-Weiss manner but becomes flatter toward lower temperatures when spin-spin correlations set in. A hump around 27 K coincides with the lattice anomaly discussed above. At even lower temperatures, $\chi(T)$ shows an upturn around 20 K and a splitting at 12 K between field-cooled (FC) and zero-field-cooled (ZFC) curves measured in a weak applied field. While the latter signature may be indicative of spin freezing, our frequency-dependent ac susceptibility measurement (see the Supplemental Material

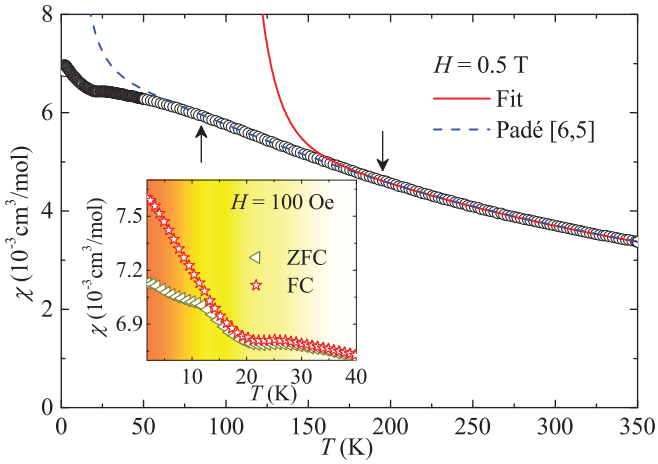

FIG. 3. Temperature dependence of magnetic susceptibility [$\chi(T)$] measured in an applied field of 0.5 T and in the temperature range $1.8 \leqslant T \leqslant 350$ K. The solid and dashed lines denote the fits by Eq. (4) and the Padé approximation, respectively. Arrows signal the limit of validity of HTSE or the Padé approximation. Inset: zero-field-cooled (ZFC) and field-cooled (FC) magnetic susceptibilities as a function of temperature measured in a field of 100 Oe.

[41]) rules out the possibility of a conventional spin-glass transition.

Traditionally, $\chi(T)$ is fitted by the sum of a temperature-independent term (χ_0) and of a Curie-Weiss law, $\chi_0 + \frac{C}{T-\theta_{CW}}$, in order to obtain the Curie constant C and the characteristic CW temperature θ_{CW}. C yields the effective moment while θ_{CW} represents the energy scale of the total exchange interactions. θ_{CW} is given by $|\theta_{CW}| = \frac{JzS(S+1)}{3k_B}$, where $z = 6$ is the number of nearest neighbors of Cr^{3+} ions and J ($= J_1$) is the intralayer exchange coupling [42]. This requires the T range of the measurements to fall into the high-temperature regime, $T \gg |\theta_{CW}|$, which is not the case here. Indeed, our $\chi(T)$ data are limited up to 350 K, and θ_{CW} for $HCrO_2$ is in the range 220–270 K [38].

We therefore used high-temperature series expansion (HTSE), now available up to 11th order [43], and Padé approximants [44] to fit our data,

$$\chi = \chi_0 + \chi_{spin}(T) \tag{4}$$

and

$$\chi_{spin}(T) = \frac{N_A g^2 \mu_B^2}{k_B T} \times \left[\frac{5}{4} - \frac{75}{8}x + \frac{225}{4}x^2 - \frac{18\,765}{64}x^3 + \frac{712\,175}{512}x^4 - \frac{6\,328\,661}{1024}x^5 + \frac{643\,219\,519}{24\,576}x^6 - \frac{36\,677\,316\,665}{344\,064}x^7 + \frac{1\,154\,751\,891\,527}{27\,525\,127}x^8 - \frac{1\,888\,217\,340\,683}{1\,179\,648}x^9 + \frac{11\,768\,319\,087\,087\,113}{1\,981\,808\,640}x^{10}\right], \tag{5}$$

with $x = \frac{J}{k_B T}$. Figure 3 depicts the fitting of $\chi(T)$ data in the validity T-range of Eq. (4), $k_B T > 8J$, corresponding to $T > 195$ K. Fixing $g = 2$ from the ESR data of Ref. [22], we obtain $J/k_B = (24 \pm 0.2)$ K and $\chi_0 = -(5.35 \pm 0.45) \times 10^{-5}$ cm^3/mol. An extension of the validity of the fit down to $T \sim 3.5J$ can be obtained using Padé approximants, which are now available. The [6,5] Padé extension of our fit is shown as a dashed blue line in Fig. 3 and perfectly matches with our data in its validity domain, $T \gtrsim 85$ K, with $J/k_B = 24$ K and $\chi_0 = -5.35 \times 10^{-5}$ cm^3/mol.

C. Heat capacity

The heat capacity (C_p) data are shown in Fig. 4 (upper panel) as a function of temperature measured in zero magnetic field. At high temperatures, $C_p(T)$ is entirely dominated by the contribution of phonon excitations (C_{ph}), and the value of C_p at 300 K is about ~62 J/mol K. This value is close to the expected Dulong-Petit lattice heat capacity of $C_v = 3nR \simeq 74.8$ J/mol K, where n is the number of atoms per formula unit [45]. In α-$HCrO_2$, H is the lightest element expected to have a very high Debye frequency compared to other elements, and therefore we chose $n = 3$ for the calculation. At around 24 K, the heat capacity shows a clear and very broad anomaly that confirms the magnetic transition. With further decrease in temperature, $C_p(T)$ decreases gradually towards zero. At low temperatures, $C_p(T)$ is dominated by the magnetic contribution C_{mag}.

To estimate the phonon part of the heat capacity, the $C_p(T)$ data were fitted above 100 K by a sum of Debye contributions

$$C_p(T) = 9R \sum_{n=1}^{3} c_n \left(\frac{T}{\theta_{Dn}}\right)^3 \int_0^{\frac{\theta_{Dn}}{T}} \frac{x^4 e^x}{(e^x - 1)^2} dx. \tag{6}$$

Here, R is the molar gas constant, θ_{Dn} are the characteristic Debye temperatures, and c_n are the integer coefficients indicating the contributions of different atoms to $C_p(T)$. A similar approach has been chosen previously to estimate the phonon contribution in different types of frustrated magnets [46]. Figure 4 (upper panel) presents the fit of $C_p(T)$ by Eq. (6) with $c_1 = 1$, $c_2 = 1$, and $c_3 = 2$. Here, c_1, c_2, and c_3 represent the number of H, Cr, and O atoms, respectively. The sum of c_n is thus equal to 4, the number of atoms per formula unit. We have used three different Debye temperatures: θ_{D1} for H^{1+}, θ_{D2} for Cr^{3+}, and θ_{D3} for O^{2-}. Finally, the high-T fit was extrapolated down to 2 K and $C_{mag}(T)$ was estimated by subtracting $C_{ph}(T)$ from $C_p(T)$ [see Fig. 4 (upper panel)].

$C_{mag}(T)/T$ is plotted as a function of temperature in the lower panel of Fig. 4. It extends up to 100 K, even though the leading exchange coupling J is about 24 K only. For the validation of the fitting procedure, we calculated the total magnetic entropy (S_{mag}) by integrating $C_{mag}(T)/T$ between 2 K and high temperatures as $S_{mag}(T) = \int_{2\,K}^{T} \frac{C_{mag}(T')}{T'} dT'$. The obtained magnetic entropy at 150 K is $S_{mag} \simeq 10.4$ J/mol K. This value of S_{mag} corresponds to ~90% (see the lower panel

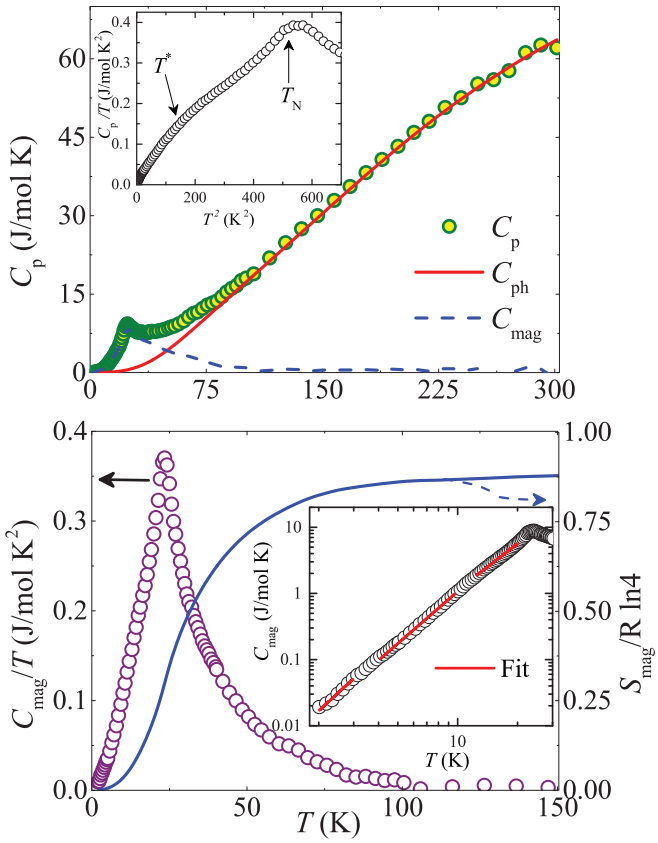

FIG. 4. Upper panel: Temperature-dependent heat capacity $C_p(T)$ of α-$HCrO_2$ measured in zero applied magnetic field. The solid line represents the simulated phonon contribution $C_{ph}(T)$ and the dashed line represents the magnetic contribution $C_{mag}(T)$. Inset: plot of $C_p(T)/T$ vs T^2 below T_N, highlighting the shoulder at $T^* \simeq 12$ K. Lower panel: C_{mag}/T and $S_{mag}/R \ln 4$ in the left and right y-axes, respectively, are plotted as a function of temperature. Inset: logarithmic plot of C_{mag} vs T, with solid lines showing the fits with a power-law, $C_{mag} = aT^{\alpha}$, in different temperature regimes.

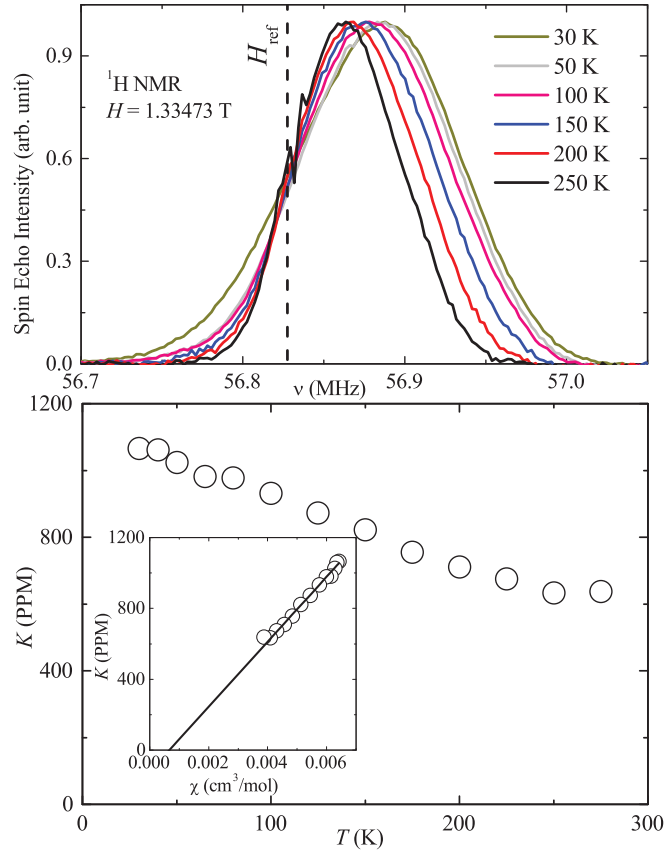

FIG. 5. Upper panel: FT ^{1}H NMR spectra at different temperatures for the polycrystalline α-$HCrO_2$ sample measured at $H =$ 1.334 73 T. The vertical dashed line corresponds to the ^{1}H resonance frequency of the nonmagnetic reference sample. Lower panel: ^{1}H NMR shift K as a function of T. Inset: ^{1}H NMR shift vs χ with temperature as an implicit parameter. The solid line represents the linear fit.

of Fig. 4) of the expected theoretical value $S_{mag} = R \ln(2S + 1) = 11.5$ J/mol K for an $S = 3/2$ system. Moreover, the entropy at T_N is found to be only one-third of the total entropy, and the remaining entropy is distributed above T_N due to short-range (in-plane) spin correlations. This is in contrast with the conventional LRO where the entropy is recovered completely just above T_N, and it confirms the strongly frustrated nature of α-$HCrO_2$ [18,47].

The broad maximum in C_{mag} around 24 K confirms the magnetic transition, whereas a broad shoulder in C_p/T versus T^2 (inset of the upper panel of Fig. 4) suggests another magnetic instability at $T^* \simeq 12$ K that coincides with the temperature at which the ZFC and FC susceptibilities bifurcate. This feature is quite similar to that reported for $CuCrO_2$ and α-$KCrO_2$ previously [24,48].

The logarithmic plot of C_{mag} versus T below T_N (see the lower inset of Fig. 4) reveals a nearly linear behavior, although a closer inspection of the data suggests that different power-law exponents are obtained in different temperature intervals. Using $C_{mag} = aT^{\alpha}$, we find $a \simeq 0.0052$ J mol^{-1} K^{-4} and $\alpha \simeq 2.2$ for $12.5 \leqslant T \leqslant 20$ K, $a \simeq 0.0026$ J mol^{-1} K^{-4} and $\alpha \simeq 2.6$ for $4 \leqslant T \leqslant 10$ K, and $a \simeq 0.0025$ J mol^{-1} K^{-4} and $\alpha \simeq 2.8$ for $2 \leqslant T \leqslant 3$ K. Considering $\alpha = 2$ and 3 expected for antiferromagnets in two and three dimensions, respectively, we conclude that spin correlations gradually evolve from a 2D behavior immediately below T_N toward a 3D behavior well below T^*.

D. ^{1}H NMR

The crystal structure of α-$HCrO_2$ [Fig. 1(c)] features a single crystallographic H site located in between two Cr-triangles. The ^{1}H nucleus is then coupled to three Cr^{3+} ions from each of the two adjacent layers. Thus, one can probe static and dynamic properties of the Cr^{3+} spins by performing ^{1}H NMR. We have measured ^{1}H NMR spectra by doing a Fourier transform of the echo signal at different temperatures, keeping the field persistent. Figure 5 (upper panel) presents the FT ^{1}H NMR spectra at different temperatures. We indeed observed a single spectral line, as expected for an $I = 1/2$ nucleus. The line position was found to increase weakly with decreasing temperature. The lower panel of Fig. 5 presents the temperature variation of the NMR shift (K) for $T > 30$ K. The slope of the linear fit using $K(T) = K_0 + \frac{A_{hf}}{N_A}\chi_{spin}(T)$ (where

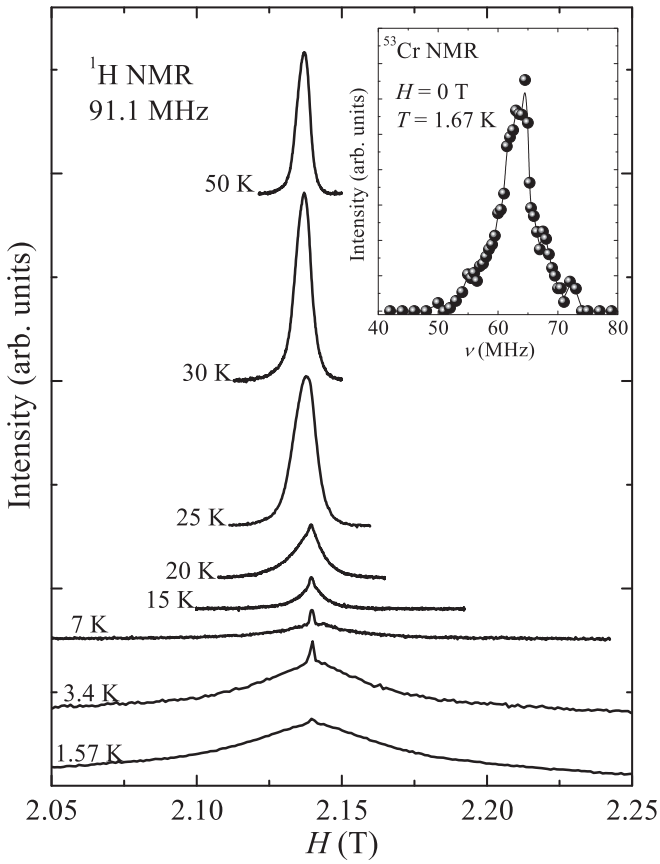

FIG. 6. Field-sweep ^{1}H NMR spectra at different temperatures around T_N measured on the polycrystalline α-$HCrO_2$ sample at 91.1 MHz. Inset: ^{31}Cr NMR spectrum at $T = 1.67$ K measured in zero field.

K_0 is the temperature-independent chemical shift) of the K versus χ plot yields the hyperfine coupling constant $A_{hf} \simeq 1024$ Oe/μ_B between the ^{1}H nucleus and the Cr^{3+} electronic spins (see the inset of Fig. 5). This value of A_{hf} is almost six times smaller than ^{7}Li in $LiCrO_2$ [18,21] but much larger than the expected dipolar coupling for α-$HCrO_2$ [49]. The latter also indicates a substantial overlap of the hydrogen 1s orbital with the 3d orbitals of the Cr^{3+} ion via 2p orbitals of O. This further explains why the interlayer exchange coupling through H is significant, as estimated in Sec. III F. Figure 6 shows the field-sweep NMR spectra around and below T_N. As the temperature approaches T_N from above, the NMR signal intensity decreases. Below T_N, the signal is reduced drastically, whereas the linewidth does not show any significant increase. The loss of the NMR signal continues well below T_N but never becomes complete, and below ~10 K the intensity quickly recovers. Below 10 K, the NMR line broadens and develops a triangular shape which is independent of the applied field. This broadening is indicative of local magnetic fields appearing at the ^{1}H site, but it is remarkable that such a broadening appears only below 10 K and not immediately below T_N, as in conventional 3D antiferromagnets. This is a clear indication that the NMR signal is wiped out over a broad temperature window, below T_N, and a pure static state appears only below 10 K. The wipe out effect is very well evident in the temperature-dependent

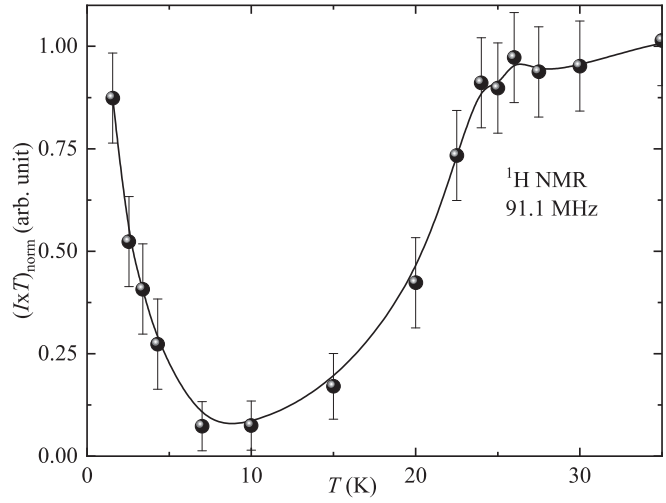

FIG. 7. Integrated NMR intensity as a function of temperature.

integrated NMR intensity plot in Fig. 7. A rectangular line shape on the polycrystalline sample is expected in an ordered collinear antiferromagnet [50,51]. The triangular line shape observed at low temperatures in α-$HCrO_2$ is reminiscent of an incommensurate magnetic order [52,53] that may appear in triangular antiferromagnets upon a distortion of the commensurate 120° state. Further, as the intrinsic signal is lost below T_N, a very narrow central line becomes prominent at the zero shift position, on top of the broad spectrum. This narrow line persists down to the lowest measured temperature, and it can be attributed to the effect of defects and/or a small amount of nonmagnetic impurities.

We have also measured the ^{53}Cr NMR ($I = 3/2$ and $\gamma_N/2\pi = 2.400\,94$ MHz/T) spectrum by sweeping the frequency in zero field at $T = 1.67$ K (see the inset of Fig. 6). The observation of the ^{53}Cr zero-field NMR signal is direct evidence of a static magnetic ordering of Cr^{3+} moments in α-$HCrO_2$ well below T^*. From the peak position, the internal field at the Cr site is estimated to be $|H_{int}| \sim 26.4$ T. Such a large value of H_{int} is comparable to the reported value ~28.64 T for $YCrO_3$ and ~27.0 T for $CuCrO_2$ [54].

E. μSR

To probe the dynamics in the fluctuating regime in more detail, we performed complementary μSR experiments. Due to its much shorter time window (10 ns–15 μs), μSR is better suited than NMR in tracking the persisting dynamics in slowly fluctuating magnets. In addition, μSR allows us to probe *all* sites, whereas only a weak fraction of the sites were detected in NMR between 20 and 3 K due to the wipeout effect.

μSR experiments under a weak applied field perpendicular to the initial muon spin polarization (wTF) were performed in order to track the spin freezing and the static magnetic volume fraction versus temperature. Indeed, only muons stopping close to paramagnetic (unfrozen) sites precess around the applied field direction and produce long-lived oscillations of the polarization reflected in the measured asymmetry. On the contrary, muons close to magnetically frozen parts experience much larger fields with a large distribution and yield a strongly

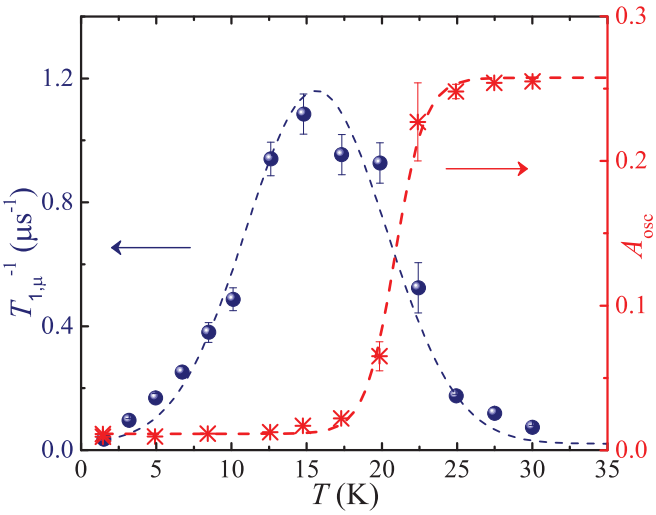

FIG. 8. Left: T-variation of the muon relaxation rate; the dashed line is a guide to the eyes. Right: weak transverse field μSR asymmetry (see text). The dashed line is a fit to a phenomenological broadened "step" function $(A_{tot} - A_b)/[1 + e^{[(T_N - T)/\Delta T_N]}] + A_b$.

damped contribution in the 0.1 μs range to the polarization, as is evident in zero-field experiments presented next.

The wTF asymmetry was fitted using a standard function for $t > 0.5$ μs,

$$A_{wTF}(t) = A_{osc}\cos(\gamma_\mu B_{ext} t + \phi)e^{-(\sigma^2 t^2/2)} + A_{tail}e^{-\lambda t}, \quad (7)$$

where A_{osc} is the wTF oscillating asymmetry and A_{tail} is introduced to account for the nonoscillating long-time relaxing frozen part ($1/3^{rd}$ tail). The fitted values for A_{osc} are shown in Fig. 8 (right). An abrupt loss of asymmetry is observed at a temperature of 22.5 K—taken as the most precise definition of T_N, within a $\Delta T_N \sim 3$ K range around T_N, indicating a uniform freezing in the sample. At lower temperatures, a constant $A_b \sim 0.01$ asymmetry is found which corresponds to ~4% muons sitting in a nonmagnetic part of the sample, possibly defects or an impurity phase. Note that this is in line with the spectral weight of the persisting narrow peak found in the NMR experiment.

Typical zero-field asymmetry curves are presented in Fig. 9. Above T_N, in the fast fluctuation regime, muons mainly sense a weak ~ 4.6 G static nuclear magnetic field mainly originating from H nuclei. The decrease of the μ^+ polarization has the expected Kubo-Toyabe shape, Gaussian at early times and modulated by a slowly exponential relaxing envelope associated with electronic spin fluctuations. When decreasing the temperature below T_N, similar to the $NaCrO_2$ case [21], the freezing of the electronic moments induces a very fast decrease of the asymmetry on a 0.1 μs range while the long-time $1/3^{rd}$ tail monitors the relaxation induced by the spin dynamics.

We first focus on the data obtained deep in the frozen regime. Figure 10 shows the very early time behavior of the asymmetry at 1.5 K. The oscillating behavior is made clear by the two visible wiggles and rules out a spin-glass-like random freezing. The damping is very large, associated with a large distribution of the field at the muon site as depicted by

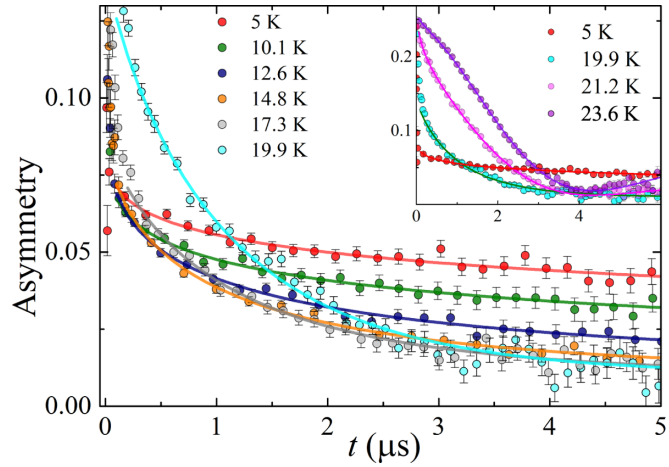

FIG. 9. μSR asymmetry in zero external field at various temperatures. The solid lines are fits described in the text.

the Fourier transform presented in the inset. Finally, one also observes the beginning of the $1/3^{rd}$ tail ($t > 0.06$ μs).

The $T = 1.5$ K asymmetry evolution with time was fitted according to the model

$$A(t) = A_0\left[\frac{2}{3}P_{osc}(t)e^{-(\sigma'^2 t^2/2)} + \frac{1}{3}\right]e^{-(t/T_1)^\alpha} + A_b, \quad (8)$$

where $P_{osc}(t)$ is an oscillating function corresponding to the μ^+ precession around the internal magnetic field (B_μ) direction at the average frequency $\nu = (\gamma_\mu/2\pi)B_\mu$, while the damping of the oscillation is due to the width of the internal field distribution σ'/γ_μ. The constant background, $A_b = 0.01$, was fixed from the remaining wTF asymmetry at $T \ll T_N$, and A_0 was set to $A_0 = A_{tot} - A_b$, with $A_{tot} = 0.255$, as determined from the total asymmetry fitted above T_N. We found a slightly better χ^2 when fitting the oscillations with a Bessel function rather than a simple cosine. A $B_\mu \sim 2.75$ kG internal field is estimated from the frequency of the oscillations. The fast early time damping reveals a large 1.4 kG HWHM

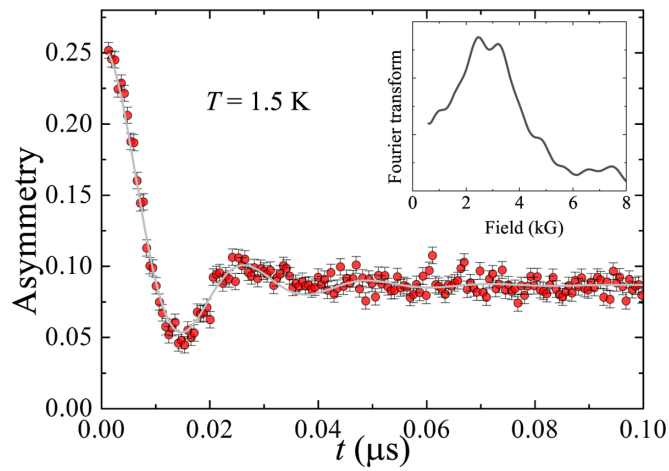

FIG. 10. Early-time μSR asymmetry in zero external field at 1.5 K and fit with a zero-order Bessel function $A[\frac{2}{3}J_0(t)e^{-\lambda t} + 1/3]$. Inset: corresponding Fourier transform after subtraction of the $1/3^{rd}$ tail.

distribution of B_μ, either associated with an incommensurate order (Bessel fit) or a sizable disorder (cosine fit). The flatness of the 1/3rd tail on the timescale of Fig. 10, hence the weakness of the relaxation rate $1/T_1$, indicates a purely static magnetic frozen phase in the low-T limit.

We now focus on the relaxation effects evidenced on the 1/3rd tail at $t > 0.1$–0.2 μs as displayed in the main panel of Fig. 9. This was the central focus of our μSR study, given the wipe-out observed in NMR. For each temperature below 19.9 K, we could estimate the "unfrozen" contribution so that the asymmetry of the corresponding 1/3rd tail was fixed from the wTF data. The asymmetry evolution with time was fitted using the following functions for $t > t_{1/3^{rd}}$ taken such that $A(t) \leqslant A_{\text{tail}}$:

$$A(t) = A_{\text{tail}}\, e^{-t/T_1{}^{\alpha}} + A_b \quad (T < T_N) \tag{9}$$

and

$$A(t) = A_0\, \text{KT}(t)\, e^{-t/T_1{}^{\alpha}} + A_b \quad (T \gtrsim T_N), \tag{10}$$

where KT(t) is the Kubo-Toyabe function, Gaussian-like in the $t \to 0$ limit, and $t_{1/3\text{rd}}$ is the time where the asymmetry falls to the value expected for the 1/3rd tail, determined as $A_{\text{tail}} + A_b$; see above. The stretched exponent α was found to vary smoothly between 12 K and up to the transition from its low-T value ~0.3 to 1. This indicates a broad distribution of relaxation times, in line with the distribution of internal fields reported in Fig. 10. The error bars mainly come from the estimate of $t > t_{1/3^{rd}}$, the error bars on the background and on the total asymmetry which slightly impact the relaxation rate. The fits were straightforward between 1.5 and 17.3 K where the "unfrozen fraction" is zero or marginal. For $T = 19.9$ K, the unfrozen part has a contribution to the relaxation which cannot be disentangled from the 1/3rd tail. A_{tail} was therefore replaced by $A_{\text{tail}} + A_{\text{osc}}$ in Eq. (9), leading to an average value of the relaxation rate. The increase of the relaxation rate is clearly visible, up to T_1^{-1} (15 K) ~ 1 μs^{-1}, followed by a decrease at $T = 17$ K (Fig. 8, left). The large T-range below T_N where slow fluctuations occur clearly signals an unconventional dynamical regime peaked around $0.7\,T_N$, at variance with the common phase transitions where the relaxation is peaked at T_N [55].

F. Microscopic analysis

DFT calculations are used to identify the trends in the microscopic magnetic parameters across the $A\text{CrO}_2$ series. Exchange couplings and single-ion anisotropies computed for LiCrO_2, NaCrO_2, α-KCrO_2, and for the two structural models of HCrO_2 are summarized in Table I. All compounds are dominated by the nearest-neighbor in-plane coupling J_1. This coupling is highly sensitive to the Cr-Cr distance d and decreases from LiCrO_2 ($d = 2.901$ Å) to NaCrO_2 ($d = 2.975$ Å) and eventually α-KCrO_2 ($d = 3.044$ Å). The J_1 value in α-HCrO_2 lies in between those of the Na and K compounds, despite its Cr-Cr distance of 2.968 Å, which is slightly shorter than in the Na case. This additional reduction in the J_1 value may be caused by the hydrogen atoms that are placed next to oxygen and change its polarization [56]. The exact position of hydrogen along the O-H-O contact ($R\bar{3}m$ versus $R3m$ models) plays only a minor role, as evident from Table I.

TABLE I. Exchange couplings J_i (in K) and single-ion anisotropy D (in K) obtained from DFT+U calculations for the spin Hamiltonian, Eq. (1). J_1, J_2, and J_3 are in-plane couplings between first, second, and third neighbors, respectively. $J_\perp$ is the frustrated interplane coupling.

	J_1	J_2	J_3	$J_\perp$	D
LiCrO_2	84	−0.3	3.6	0.4	0.4
NaCrO_2	48	−0.5	2.7	0.1	0.6
α-KCrO_2	15	0.6	4.1	0.2	0.9
α-HCrO_2, $R\bar{3}m$	33	−0.2	4.3	2.8	0.5
α-HCrO_2, $R3m$	28	1.0	4.3	2.0	0.5

The computed values of J_1 are generally in good agreement with the experimental estimates based on the magnetic susceptibility data (Table II). The coupling in LiCrO_2 is also in accord with the spectroscopic measurements of magnetic excitations [57] that suggested $J_1 \simeq 70$ K (6.0 meV).

A weak easy-axis single-ion anisotropy (D) is present in all compounds and does not change significantly across the series. Indeed, the calculated value of D for α-KCrO_2 matches well with the value estimated from the ESR experiments (see the Supplemental Material [41]). On the other hand, the interlayer coupling $J_\perp$ notably increases in α-HCrO_2, due to the reduced interlayer spacing (Table II) and the covalent nature of the O-H bonds as opposed to the purely ionic bonding between alkali metals (Li, Na, and K) and oxygen.

IV. DISCUSSION

This section is divided into two parts: the first part is devoted to a discussion on the transition temperature with respect to frustration. The second part is devoted to the extended dynamical regime below the transition, which is found to have a universal character among the $A\text{CrO}_2$ (A = H, Na, and K) series of chromates.

For a purely 2D triangular Heisenberg antiferromagnet, one would expect a transition only at $T = 0$ into a three-sublattice structure with spins at 120°. In the presence of a weak interlayer exchange coupling, the transition is still mainly driven by the growth of the 2D correlation length $\xi(T)$ when cooling down: it diverges at $T = 0$. Indeed, in a mean-field approach, the transition is obtained by equating the thermal energy to the interaction of 2D correlated patches

TABLE II. Comparison of different structural and magnetic parameters of $A\text{CrO}_2$ (A = H, Li, Na, and K) [58]. The exchange coupling J ($= J_1$) for Li, Na, and K compounds is deduced using the HTSE given by Delmas *et al.* [59], whereas for α-HCrO_2 we have used 11th-order HTSE [Eq. (5)] suggested by Schmidt *et al.* [43].

Compounds	Interplanar spacing (Å)	J (K)	T_N (K)	Refs.
α-HCrO_2	4.774	24	22.5	This work
LiCrO_2	4.807	78	62	[22,24]
NaCrO_2	5.323	40	41	[21,22]
α-KCrO_2	5.963	24	23	[24,60]

through a small interlayer exchange coupling. This can be approached by the following mean-field equation that leads to a finite transition temperature,

$$k_B T_N \sim J_\perp S^2 [\xi(T_N)/a]^2. \quad (11)$$

From Refs. [61,62] we get

$$\xi(T) \sim (T/J)^{-0.5} \exp(\alpha J/T). \quad (12)$$

One can then expect a transition temperature modestly increasing with $J_\perp$. From Tables I and II, one can notice that $J_\perp$ decreases when the interlayer distance increases from α-$HCrO_2$ to α-$KCrO_2$, as expected, and $J_\perp$ is more than a factor 15–30 larger for α-$HCrO_2$ as compared to $NaCrO_2$ and α-$KCrO_2$. While the J/T_N ratio is similar or even slightly larger for α-$HCrO_2$, the transition temperature surprisingly does not scale at all with $J_\perp$. We suggest that this failure of the mean-field, well-established, approach for low-dimensional systems can be assigned to a peculiar degree of interlayer frustration in α-$HCrO_2$. Indeed, we first note that the geometry of the interlayer coupling [see Fig. 1(b)] leads to some frustration through the *tetrahedral* units resulting from the *ABC* type of stacking, common to all the chromates mentioned above: one Cr^{3+} is coupled to six Cr^{3+} from the two adjacent layers. Second, a higher degree of frustration induced by the interlayer coupling, as found for α-$HCrO_2$, certainly prevents the correlation length from growing according to Eq. (12), which leads to the apparent paradox of "a larger $J_\perp$ yields to a lower T_N." We note that this frustration scenario is in line with the incommensurate structure observed at 1.57 K through the NMR line shape and also consistent with the μSR time evolution of the asymmetry at 1.5 K.

Now, coming to the intermediate T-range below T_N, several of the $ACrO_2$ compounds show a very similar phenomenology. In Fig. 11, we compare our results to those obtained in $NaCrO_2$ [21], using J as a scaling parameter.

(i) Both α-$HCrO_2$ and $NaCrO_2$ undergo a magnetic transition that manifests itself in the heat capacity and μSR, but it does not lead to the formation of a conventional 3D transition with a narrow critical regime centered in the vicinity of T_N. On the contrary, here the transition at T_N is followed by a broad regime with slow fluctuations peaked around 0.6–0.7 T_N [Fig. 11(c)]. Strikingly, this maximum largely coincides with the bifurcation point of the FC/ZFC susceptibility reported at 12–15 K in Fig. 3 for α-$HCrO_2$. The extension of this regime can be tracked through the μSR relaxation rate, which shows a striking similarity in both compounds once the temperatures are normalized by J.

(ii) The heat capacity also displays a very broad maximum around T_N and a similar behavior below T_N for both compounds when the temperature axis is scaled by their respective J.

(iii) For both compounds, the intensity of the NMR line progressively decreases, goes through a minimum, and recovers below a temperature T^* where slow fluctuations detected through μSR freeze out [63].

Similar plots including the data taken on α-$KCrO_2$ can be found in the Supplemental Material [41]. They clearly demonstrate the universal character of this scaling in T/J for that series of chromates.

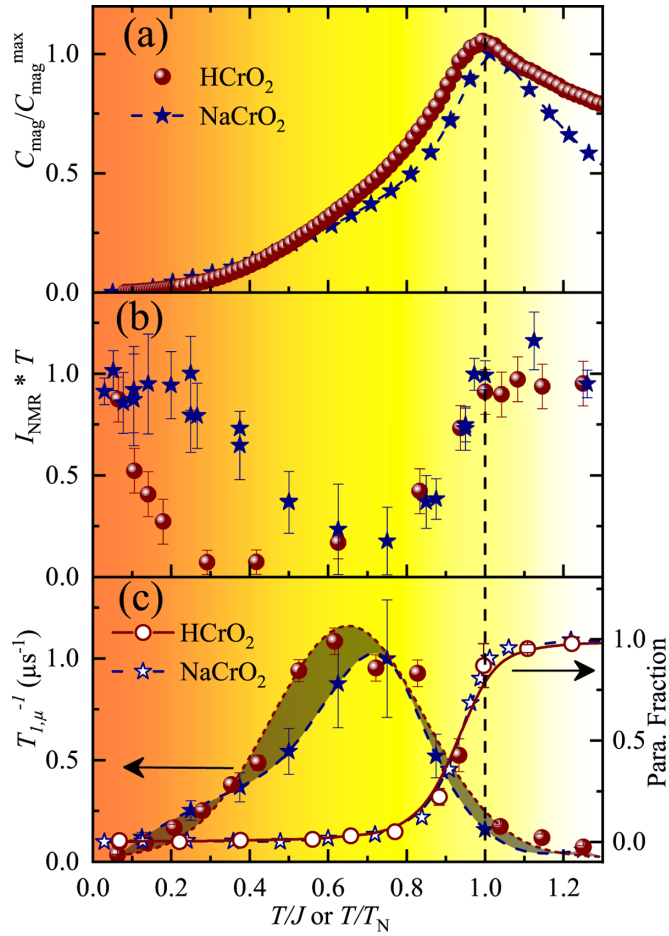

FIG. 11. Comparison of low-temperature data of α-$HCrO_2$ with $NaCrO_2$; (a) magnetic heat capacity normalized to its maximum value vs T/J, (b) evaluation of integrated NMR intensity with T/J, and (c) μSR relaxation rate $1/T_{1,\mu}$ vs T/J and the paramagnetic fraction vs T/T_N in the left and right y-axes, respectively. Here the transition temperature is taken to be $T_N \simeq 22.5$ and 41 K for α-$HCrO_2$ and $NaCrO_2$, respectively.

We are therefore led to the conclusion that a broad universal dynamical regime emerges on a T/J scale, typical of *ABC*-stacked triangular Heisenberg antiferromagnets and characterized by a very progressive slowing down of spin fluctuations.

Neutron scattering studies offered a possible explanation for this unusual behavior as reported earlier for $NaCrO_2$ [64–66]. Between 1.3 and 0.7 T_N, the in-plane correlation length grows rapidly with a $\vec{q}$ vector typical of the 120° pattern. On the contrary, the interlayer correlation length increases very progressively from one interlayer spacing at T_N to only four interlayer spacings at 0.7 T_N where it levels off. This T-range closely below T_N is dominated by 2D correlations.

The increase in $1/T_{1,\mu}$ up to its maximum could be such a hallmark of the 2D regime, in fair agreement with the T^2 behavior of the specific heat that we clearly observe in α-$HCrO_2$. At lower temperatures, a release of the interlayer frustration through a small incommensuration may strengthen the 3D coupling. The consequence is a progressive slowing down of

the fluctuations as observed in μSR. This regime is typical of a 2D-3D crossover. What remains unclear is certainly the universality observed in the maximum of $1/T_{1,\mu}$. It might be a coincidental result of two counteracting mechanisms driven by $J_\perp$, namely, an increase of both the coupling and the frustration between the layers.

Alternative scenarios, namely the Berezinskii-Kosterlitz-Thouless (BKT) scenario of vortex-antivortex binding or that of Z_2 vortex excitations, have been proposed for $NaCrO_2$ [21,22]. Indeed, the maximum in the μSR relaxation rate at $T_m \simeq 0.7\ T_N$ was found to coincide with the divergence of the correlation length inferred from the broadening of the ESR line according to the BKT model, $\xi(T) \sim \exp \frac{b}{T-T_m}$. The data now available on α-$HCrO_2$ and α-$KCrO_2$ prove the failure of this scaling in T/T_m (see the Supplemental Material [41] for the tentative scaling) and rule out such an interpretation. In addition, we note that a BKT scenario requires a substantial XY anisotropy, which has never been observed experimentally. This, therefore, calls for a different interpretation of the ESR line broadening in terms of a growth of the correlation length when entering the 3D regime.

A more general lesson from the $ACrO_2$ chromates is that the fluctuating 2D regime clearly sets in below T_N, likely from the interlayer frustration. This offers a new perspective on the persistent spin dynamics and other spin-liquid phenomenology such as observed in the $AYbX_2$ compounds [15,16] where exchange anisotropy also certainly plays a role. It also calls for the improved theoretical understanding of how deep the frustration of weak interlayer couplings may affect the ground state of a quasi-2D antiferromagnet. Our experimental data for the pure Heisenberg triangular chromates set an important benchmark for such studies.

In conclusion, besides the observation of a Néel transition, features reminiscent of the pure 2D Heisenberg triangular lattice are manifested through the dynamics as revealed here experimentally, between T_N and $0.7\ T_N$. The study of the $ACrO_2$ chromates (A = H, Na, and K) points to an original and universal character of excitations. With their half-filled t_{2g} orbitals, chromates are certainly the best representative of a semiclassical $S = 3/2$ Heisenberg model. The perfection of the equilateral triangular lattice with almost no disorder is a strong asset to provide a solid playground for the physics of frustration at play on the triangular lattice in a context where more disordered compounds such as $YbMgGaO_4$ or $AYbX_2$ QSL candidates are in the spotlight. Certainly, the interpretation of the 2D-3D crossover resides in the details of each of these compounds, although the universal plot in T/J might suggest that it is still governed by the dynamics specific to the 2D frustrated character of the triangular lattice.

V. SUMMARY

The static and dynamic properties of spin-3/2 TLHAF α-$HCrO_2$ are studied in detail and compared with the isostructural compounds (Na,K)CrO_2. $\chi(T)$ could be modeled using HTSE for spin-3/2 TLHAF, which yields an intralayer coupling $J/k_B \simeq 24$ K. The complementary band-structure calculations result in a similar value of J. They additionally provide a sizable interlayer coupling $J_\perp/k_B \simeq 2.8$ K, which appears specific to α-$HCrO_2$. This brings in interlayer frustration which shifts down the transition temperature as compared to other members of the chromates series. On the experimental side, a large hyperfine coupling $A_{hf} \simeq 1021$ Oe/μ_B between the ^{1}H nuclei and the Cr^{3+} spins corroborates the existence of such a sizable interlayer coupling.

Although $\chi(T)$, $C_p(T)$, and muon asymmetry measurements reveal the onset of a magnetic transition at T_N, which is also monitored through a magnetoelastic coupling, a wide fluctuating crossover regime marked by a broad peak in the muon relaxation rate $1/T_{1,\mu}$ centered at $T \simeq 0.7\ T_N$ and a minimum in the ^{1}H NMR integrated intensity is singled out. Apparently, this slow dynamical regime turns out to be a universal character of the TLHAFs $ACrO_2$ (A = Na, K, and H) when the specific heat, NMR intensity, $1/T_{1,\mu}$, and paramagnetic fraction are plotted against the scaled (with respect to J or T_N) temperature. This supports a scenario where a crossover from 2D to 3D correlations sets in around $0.7\ T_N$ preceded by a typical 2D regime of the TLHAF.

ACKNOWLEDGMENTS

P.M. and R.N. thank J. Richter for discussions and for providing the HTSE and Padé approximants used in the fit of our susceptibility data. K.S. and R.N. would like to acknowledge SERB, India for financial support bearing sanction Grant No. CRG/2019/000960. The work in Augsburg was supported by the German Research Foundation (DFG) via Project No. 107745057 (TRR80). Work at the Ames Laboratory was supported by the U.S. Department of Energy, Office of Science, Basic Energy Sciences, Materials Sciences, and Engineering Division. The Ames Laboratory is operated for the U.S. Department of Energy by Iowa State University under Contract No. DEAC02-07CH11358. F.B., P.M., and G.S. acknowledge the support of the French Agence Nationale de la Recherche under Grant No. ANR-18-CE30-0022. The work of G.S. is funded by the Swiss National Science Foundation Mobility grant P2EZP2-178604 and PALM LabEx grant ANR-10-LABX-0039-PALM. Part of this work is based on experiments performed at the Swiss Muon Source SμS, Paul Scherrer Institute, Villigen, Switzerland. We would like to thank A. Amato and C. Wang for the technical assistance with the GPS spectrometer. We thank C. Delmas (ICMCB, Bordeaux) for providing the $KCrO_2$ sample, and N. Penin for mounting it. We thank A. Ozarowski for technical assistance with ESR measurements. A.Z. acknowledges the financial support of the Slovenian Research Agency through program No. P1-0125 and projects No. BI-US/18-20-064, No. J1-2461, and No. N1-0148. The National High Magnetic Field Laboratory where the ESR investigation was conducted is supported by National Science Foundation through NSF/DMR-1644779 and the State of Florida.

[1] C. Broholm, R. J. Cava, S. A. Kivelson, D. G. Nocera, M. R. Norman, and T. Senthil, Quantum spin liquids, Science **367**, eaay0668 (2020).

[2] J. Knolle and R. Moessner, A field guide to spin liquids, Annu. Rev. Condens. Matter Phys. **10**, 451 (2019).

[3] X.-G. Wen, Choreographed entanglement dances: Topological states of quantum matter, Science **363**, eaal3099 (2019).

[4] J. R. Chamorro, T. M. McQueen, and T. T. Tran, Chemistry of quantum spin liquids, Chem. Rev. **121**, 2898 (2021).

[5] P. Mendels and F. Bert, Quantum kagome frustrated antiferromagnets: One route to quantum spin liquids, C. R. Phys. **17**, 455 (2016).

[6] Y. Li, P. Gegenwart, and A. A. Tsirlin, Spin liquids in geometrically perfect triangular antiferromagnets, J. Phys.: Condens. Matter **32**, 224004 (2020).

[7] S. M. Winter, A. A. Tsirlin, M. Daghofer, J. van den Brink, Y. Singh, P. Gegenwart, and R. Valentí, Models and materials for generalized Kitaev magnetism, J. Phys.: Condens. Matter **29**, 493002 (2017).

[8] W. W. Liu, Z. Zhang, J. T. Ji, Y. X. Liu, J. S. Li, X. Wang, H. Lei, G. Chen, and Q. M. Zhang, Rare-earth chalcogenides: A large family of triangular lattice spin liquid candidates, Chin. Phys. Lett. **35**, 117501 (2018).

[9] M. Baenitz, P. Schlender, J. Sichelschmidt, Y. A. Onykiienko, Z. Zangeneh, K. M. Ranjith, R. Sarkar, L. Hozoi, H. C. Walker, J.-C. Orain, H. Yasuoka, J. van den Brink, H. H. Klauss, D. S. Inosov, and T. Doert, $NaYbS_2$: A planar spin-$\frac{1}{2}$ triangular-lattice magnet and putative spin liquid, Phys. Rev. B **98**, 220409(R) (2018).

[10] K. M. Ranjith, D. Dmytriieva, S. Khim, J. Sichelschmidt, S. Luther, D. Ehlers, H. Yasuoka, J. Wosnitza, A. A. Tsirlin, H. Kühne, and M. Baenitz, Field-induced instability of the quantum spin liquid ground state in the $J_{\text{eff}} = \frac{1}{2}$ triangular-lattice compound $NaYbO_2$, Phys. Rev. B **99**, 180401(R) (2019).

[11] K. M. Ranjith, S. Luther, T. Reimann, B. Schmidt, P. Schlender, J. Sichelschmidt, H. Yasuoka, A. M. Strydom, Y. Skourski, J. Wosnitza, H. Kühne, T. Doert, and M. Baenitz, Anisotropic field-induced ordering in the triangular-lattice quantum spin liquid $NaYbSe_2$, Phys. Rev. B **100**, 224417 (2019).

[12] R. Sarkar, P. Schlender, V. Grinenko, E. Haeussler, P. J. Baker, T. Doert, and H.-H. Klauss, Quantum spin liquid ground state in the disorder free triangular lattice $NaYbS_2$, Phys. Rev. B **100**, 241116(R) (2019).

[13] M. M. Bordelon, C. Liu, L. Posthuma, P. M. Sarte, N. P. Butch, D. M. Pajerowski, A. Banerjee, L. Balents, and S. D. Wilson, Spin excitations in the frustrated triangular lattice antiferromagnet $NaYbO_2$, Phys. Rev. B **101**, 224427 (2020).

[14] P.-L. Dai, G. Zhang, Y. Xie, C. Duan, Y. Gao, Z. Zhu, E. Feng, Z. Tao, C.-L. Huang, H. Cao, A. Podlesnyak, G. E. Granroth, M. S. Everett, J. C. Neuefeind, D. Voneshen, S. Wang, G. Tan, E. Morosan, X. Wang, H.-Q. Lin *et al.*, Spinon Fermi Surface Spin Liquid in a Triangular Lattice Antiferromagnet $NaYbSe_2$, Phys. Rev. X **11**, 021044 (2021).

[15] L. Ding, P. Manuel, S. Bachus, F. Grußler, P. Gegenwart, J. Singleton, R. D. Johnson, H. C. Walker, D. T. Adroja, A. D. Hillier, and A. A. Tsirlin, Gapless spin-liquid state in the structurally disorder-free triangular antiferromagnet $NaYbO_2$, Phys. Rev. B **100**, 144432 (2019).

[16] M. M. Bordelon, E. Kenney, C. Liu, T. Hogan, L. Posthuma, M. Kavand, Y. Lyu, M. Sherwin, N. P. Butch, C. Brown, M. J. Graf, L. Balents, and S. D. Wilson, Field-tunable quantum disordered ground state in the triangular-lattice antiferromagnet $NaYbO_2$, Nat. Phys. **15**, 1058 (2019).

[17] H. Kadowaki, H. Takei, and K. Motoya, Double-Q 120° structure in the Heisenberg antiferromagnet on rhombohedrally stacked triangular lattice $LiCrO_2$, J. Phys.: Condens. Matter **7**, 6869 (1995).

[18] L. K. Alexander, N. Büttgen, R. Nath, A. V. Mahajan, and A. Loidl, ^{7}Li NMR studies on the triangular lattice system $LiCrO_2$, Phys. Rev. B **76**, 064429 (2007).

[19] J. Sugiyama, M. Månsson, Y. Ikedo, T. Goko, K. Mukai, D. Andreica, A. Amato, K. Ariyoshi, and T. Ohzuku, μ^+SR investigation of local magnetic order in $LiCrO_2$, Phys. Rev. B **79**, 184411 (2009).

[20] A. Olariu, P. Mendels, F. Bert, L. K. Alexander, A. V. Mahajan, A. D. Hillier, and A. Amato, Spin dynamics in Heisenberg triangular antiferromagnets: A μSR study of $LiCrO_2$, Phys. Rev. B **79**, 224401 (2009).

[21] A. Olariu, P. Mendels, F. Bert, B. G. Ueland, P. Schiffer, R. F. Berger, and R. J. Cava, Unconventional Dynamics in Triangular Heisenberg Antiferromagnet $NaCrO_2$, Phys. Rev. Lett. **97**, 167203 (2006).

[22] M. Hemmida, H.-A. Krug von Nidda, N. Büttgen, A. Loidl, L. K. Alexander, R. Nath, A. V. Mahajan, R. F. Berger, R. J. Cava, Y. Singh, and D. C. Johnston, Vortex dynamics and frustration in two-dimensional triangular chromium lattices, Phys. Rev. B **80**, 054406 (2009).

[23] J. Liu, B. Liu, L. Yuan, B. Li, L. Xie, X. Chen, H. Zhang, D. Xu, W. Tong, J. Wang, and Y. Li, Frustrated magnetism of the triangular-lattice antiferromagnets α-CrOOH and α-CrOOD, New J. Phys. **23**, 033040 (2021).

[24] F. Xiao, T. Lancaster, P. J. Baker, F. L. Pratt, S. J. Blundell, J. S. Möller, N. Z. Ali, and M. Jansen, Magnetic transition and spin dynamics in the triangular Heisenberg antiferromagnet α-$KCrO_2$, Phys. Rev. B **88**, 180401(R) (2013).

[25] A. Amato, H. Luetkens, K. Sedlak, A. Stoykov, R. Scheuermann, M. Elender, A. Raselli, and D. Graf, The new versatile general purpose surface-muon instrument (GPS) based on silicon photomultipliers for μ^+SR measurements on a continuous-wave beam, Rev. Sci. Instrum. **88**, 093301 (2017).

[26] K. Koepernik and H. Eschrig, Full-potential nonorthogonal local-orbital minimum-basis band-structure scheme, Phys. Rev. B **59**, 1743 (1999).

[27] J. P. Perdew, K. Burke, and M. Ernzerhof, Generalized Gradient Approximation Made Simple, Phys. Rev. Lett. **77**, 3865 (1996).

[28] O. Janson, S. Chen, A. A. Tsirlin, S. Hoffmann, J. Sichelschmidt, Q. Huang, Z.-J. Zhang, M.-B. Tang, J.-T. Zhao, R. Kniep, and H. Rosner, Structure and magnetism of $Cr_2[BP_3O_{12}]$: Towards the quantum-classical crossover in a spin-3/2 alternating chain, Phys. Rev. B **87**, 064417 (2013).

[29] O. Janson, G. Nénert, M. Isobe, Y. Skourski, Y. Ueda, H. Rosner, and A. A. Tsirlin, Magnetic pyroxenes $LiCrGe_2O_6$ and $LiCrSi_2O_6$: Dimensionality crossover in a nonfrustrated $S = \frac{3}{2}$ Heisenberg model, Phys. Rev. B **90**, 214424 (2014).

[30] Z. Lu and J. R. Dahn, Structure and electrochemistry of layered $Li[Cr_xLi_{(1/3-x/3)}Mn_{(2/3-2x/3)}]O_2$, J. Electrochem. Soc. **149**, A1454 (2002).

[31] W. Scheld and R. Hoppe, Über den α-$NaFeO_2$-Typ: Zur Kenntnis von $NaCrO_2$ und $KCrO_2$, Z. Anorg. Allg. Chem. **568**, 151 (1989).

[32] M. Ichikawa, T. Gustafsson, I. Olovsson, and T. Tsuchida, Powder neutron-diffraction profile analysis of zero-dimensional H-bonded crystal $HCrO_2$, J. Phys. Chem. Solids. **60**, 1875 (1999).

[33] H. J. Xiang, E. J. Kan, S.-H. Wei, M.-H. Whangbo, and X. G. Gong, Predicting the spin-lattice order of frustrated systems from first principles, Phys. Rev. B **84**, 224429 (2011).

[34] J. Rodríguez-Carvajal, Recent advances in magnetic structure determination by neutron powder diffraction, Phys. B **192**, 55 (1993).

[35] T. Chatterji, B. Ouladdiaf, P. F. Henry, and D. Bhattacharya, Magnetoelastic effects in multiferroic $YMnO_3$, J. Phys.: Condens. Matter **24**, 336003 (2012).

[36] S. Reschke, A. A. Tsirlin, N. Khan, L. Prodan, V. Tsurkan, I. Kézsmárki, and J. Deisenhofer, Structure, phonons, and orbital degrees of freedom in $Fe_2Mo_3O_8$, Phys. Rev. B **102**, 094307 (2020).

[37] S. S. Islam, K. M. Ranjith, M. Baenitz, Y. Skourski, A. A. Tsirlin, and R. Nath, Frustration of square cupola in $Sr(TiO)Cu_4(PO_4)_4$, Phys. Rev. B **97**, 174432 (2018).

[38] R. G. Meisenheimer and J. D. Swalen, Magnetic properties of $HCrO_2$ and $DCrO_2$, Phys. Rev. **123**, 831 (1961).

[39] J. A. Ibers, C. H. Holm, and C. R. Adams, Proton magnetic resonance study of polycrystalline $HCrO_2$, Phys. Rev. **121**, 1620 (1961).

[40] T. Matsuo, T. Maekawa, A. Inaba, O. Yamamuro, M. Ohama, M. Ichikawa, and T. Tsuchida, Isotope-dependent crystalline phases at ambient temperature: Spectroscopic and calorimetric evidence for a deuteration-induced phase transition at 320 K in α-$DCrO_2$, J. Mol. Struct. **790**, 129 (2006).

[41] See Supplemental Material at http://link.aps.org/supplemental/10.1103/PhysRevB.104.104422 for additional information, which includes Refs. [22,67–74].

[42] C. Domb and A. R. Miedema, Prog. Low Temp. Phys. **4**, 296 (1964).

[43] H.-J. Schmidt, A. Lohmann, and J. Richter, Eighth-order high-temperature expansion for general Heisenberg Hamiltonians, Phys. Rev. B **84**, 104443 (2011).

[44] A. Lohmann, H.-J. Schmidt, and J. Richter, Tenth-order high-temperature expansion for the susceptibility and the specific heat of spin-s Heisenberg models with arbitrary exchange patterns: Application to pyrochlore and kagome magnets, Phys. Rev. B **89**, 014415 (2014).

[45] R. K. Fitzgerel and F. H. Verhoek, The law of Dulong and Petit, J. Chem. Ed. **37**, 545 (1960).

[46] N. Ahmed, A. A. Tsirlin, and R. Nath, Multiple magnetic transitions in the spin-$\frac{1}{2}$ chain antiferromagnet $SrCuTe_2O_6$, Phys. Rev. B **91**, 214413 (2015).

[47] H. Takatsu, H. Yoshizawa, S. Yonezawa, and Y. Maeno, Critical behavior of the metallic triangular-lattice Heisenberg antiferromagnet $PdCrO_2$, Phys. Rev. B **79**, 104424 (2009).

[48] T. Okuda, Y. Beppu, Y. Fujii, T. Onoe, N. Terada, and S. Miyasaka, Specific heat of delafossite oxide $CuCr_{1-x}Mg_xO_2$ ($0 \leqslant x \leqslant 0.03$), Phys. Rev. B **77**, 134423 (2008).

[49] The dipolar coupling constant at the H site is calculated using a lattice sum with an assumption of $1\mu_B$ magnetic moment on each Cr^{3+} ion to be $\sim$0.150 kOe/μ_B per Cr^{3+} ion.

[50] J. Kikuchi, K. Ishiguchi, K. Motoya, M. Itoh, K. Inari, N. Eguchi, and J. Akimitsu, NMR and neutron scattering studies of quasi one-dimensional magnet CuV_2O_6, J. Phys. Soc. Jpn. **69**, 2660 (2000).

[51] R. Nath, K. M. Ranjith, B. Roy, D. C. Johnston, Y. Furukawa, and A. A. Tsirlin, Magnetic transitions in the spin-$\frac{5}{2}$ frustrated magnet $BiMn_2PO_6$ and strong lattice softening in $BiMn_2PO_6$ and $BiZn_2PO_6$ below 200 K, Phys. Rev. B. **90**, 024431 (2014).

[52] M. Kontani, T. Hioki, and Y. Masuda, Hyperfine fields in an incommensurate antiferromagnetic Cr-Mo alloy system, J. Phys. Soc. Jpn. **39**, 672 (1975).

[53] K. M. Ranjith, R. Nath, M. Majumder, D. Kasinathan, M. Skoulatos, L. Keller, Y. Skourski, M. Baenitz, and A. A. Tsirlin, Commensurate and incommensurate magnetic order in spin-1 chains stacked on the triangular lattice in $Li_2NiW_2O_8$, Phys. Rev. B **94**, 014415 (2016).

[54] H. Takeda, Y. Shimizu, M. Itoh, M. Isobe, and Y. Ueda, Local electronic state in the high-valence hollandite-type chromium oxide $K_2Cr_8O_{16}$ investigated by ^{53}Cr NMR, Phys. Rev. B **88**, 165107 (2013); A. G. Smol'nikov, V. V. Ogloblichev, S. V. Verkhovskii, K. N. Mikhalev, A. Y. Yakubovskii, K. Kumagai, Y. Furukawa, A. F. Sadykov, Y. V. Piskunov, A. P. Gerashchenko, S. N. Barilo, and S. V. Shiryaev, ^{53}Cr NMR study of $CuCrO_2$ multiferroic, JETP Lett. **102**, 674 (2015).

[55] Note that the ratio of the NMR and μ SR relaxation rates $(1/T_1)_{NMR}/(1/T_1)_{\mu SR}$ scales with the ratio of the coupling constants squared. An order of magnitude can be calculated from the ratio of μSR internal field found at 1.5 K and the product of the hyperfine constant by the Cr^{3+} moment, assumed to be $3.87\mu_B$ or accordingly from the 5 kG HWHM of the NMR spectrum at 1.5 K. At 15 K, this yields a rough estimate of $(T_1)_{NMR}$, of the order of 9–25μs, which explains well the wipeout.

[56] S. Lebernegg, A. A. Tsirlin, O. Janson, and H. Rosner, Two energy scales of spin dimers in clinoclase $Cu_3(AsO_4)(OH)_3$, Phys. Rev. B **87**, 235117 (2013).

[57] S. Tóth, B. Wehinger, K. Rolfs, T. Birol, U. Stuhr, H. Takatsu, K. Kimura, T. Kimura, H. M. Rønnow, and C. Rüegg, Electromagnon dispersion probed by inelastic X-ray scattering in $LiCrO_2$, Nat. Commun. **7**, 13547 (2016).

[58] S. Angelov and J. Doumerc, On the correlation between the structure and the exchange interactions in $ACrO_2$ chromites, Solid State Commun. **77**, 213 (1991).

[59] J.-P. Doumerc, A. Wichainchai, A. Ammar, M. Pouchard, and P. Hagenmuller, On magnetic properties of some oxides with delafossite-type structure, Mater. Res. Bull. **21**, 745 (1986).

[60] N. Zafar Ali, J. Nuss, and M. Jansen, A new polymorph of potassium chromate(III), β-$KCrO_2$, and reinvestigation of α-$KCrO_2$, Z. Anorg. Allg. Chem **639**, 241 (2013).

[61] P. Azaria, B. Delamotte, and D. Mouhanna, Low-Temperature Properties of Two-Dimensional Frustrated Quantum Antiferromagnets, Phys. Rev. Lett. **68**, 1762 (1992).

[62] N. Elstner, R. R. P. Singh, and A. P. Young, Finite Temperature Properties of the Spin-1/2 Heisenberg Antiferromagnet on the Triangular Lattice, Phys. Rev. Lett. **71**, 1629 (1993).

[63] Note that the difference in the extension of this regime can be due in the way extrapolations of transverse relaxation T_2 plots have been performed, which is always fairly delicate when T_2 is short.

[64] D. Hsieh, D. Qian, R. F. Berger, R. J. Cava, J. W. Lynn, Q. Huang, and M. Z. Hasan, Magnetic excitations in triangular lattice $NaCrO_2$, J. Phys. Chem. Solids **69**, 3174 (2008).

[65] D. Hsieh, D. Qian, R. F. Berger, R. J. Cava, J. W. Lynn, Q. Huang, and M. Z. Hasan, Unconventional spin order in the triangular lattice system $NaCrO_2$: A neutron scattering study, Phys. B **403**, 1341 (2008).

[66] D. Hsieh, D. Qian, R. F. Berger, C. Liu, B. Ueland, P. Schiffer, Q. Huang, R. J. Cava, J. W. Lynn, and M. Hasan, Spin order by quantum frustration in triangular lattice Mott insulator $NaCrO_2$: A neutron scattering study, arXiv:1405.6184.

[67] T. Moriya, Nuclear magnetic relaxation in antiferromagnetics, Prog. Theor. Exp. Phys. **16**, 23 (1956).

[68] D. Beeman and P. Pincus, Nuclear spin-lattice relaxation in magnetic insulators, Phys. Rev. **166**, 359 (1968).

[69] M. Majumder, M. Prinz-Zwick, S. Reschke, A. Zubtsovskii, T. Dey, F. Freund, N. Büttgen, A. Jesche, I. Kézsmárki, A. A. Tsirlin, and P. Gegenwart, Field evolution of low-energy excitations in the hyperhoneycomb magnet β-Li_2IrO_3, Phys. Rev. B **101**, 214417 (2020).

[70] G. E. Pake, *Paramagnetic Resonance: An Introductory Monograph* (Benjamin, New York, 1962), Vol. 1.

[71] S. Angelov, J. Darriet, C. Delmas, and G. L. Flem, Relation between the EPR linewidths and the exchange integrals in $ACrO_2$ (A= Li, Na, and K), Solid State Commun. **50**, 345 (1984).

[72] R. Kubo and K. Tomita, A general theory of magnetic resonance absorption, J. Phys. Soc. Jpn. **9**, 888 (1954).

[73] A. Zorko, in *Determination of Magnetic Anisotropy by EPR*, edited by A. M. Maghraby, Topics from EPR Research (IntechOpen, London, 2019).

[74] A. Zorko, M. Pregelj, A. Potočnik, J. van Tol, A. Ozarowski, V. Simonet, P. Lejay, S. Petit, and R. Ballou, Role of Antisymmetric Exchange in Selecting Magnetic Chirality in $Ba_3NbFe_3Si_2O_{14}$, Phys. Rev. Lett. **107**, 257203 (2011).